

# Tectonics

## RESEARCH ARTICLE

10.1029/2020TC006631

### Key Points:

- We document normal fault growth in the Exmouth Plateau, offshore Australia
- Faults follow a three-stage growth model: lengthening stage, throw accumulation stage, and tip retreat stage
- We suggest tip retreat may be an important stage of normal fault growth

### Supporting Information:

Supporting Information may be found in the online version of this article.

### Correspondence to:

B. A. Lathrop,  
[b.lathrop17@imperial.ac.uk](mailto:b.lathrop17@imperial.ac.uk)

### Citation:

Lathrop, B. A., Jackson, C. A.-L., Bell, R. E., & Rotevatn, A. (2021). Normal fault kinematics and the role of lateral tip retreat: An example from offshore NW Australia. *Tectonics*, *40*, e2020TC006631. <https://doi.org/10.1029/2020TC006631>

Received 30 MAY 2020  
Accepted 28 MAR 2021

© Wiley Periodicals LLC. The Authors. This is an open access article under the terms of the [Creative Commons Attribution License](#), which permits use, distribution and reproduction in any medium, provided the original work is properly cited.

## Normal Fault Kinematics and the Role of Lateral Tip Retreat: An Example From Offshore NW Australia

Bailey A. Lathrop<sup>1</sup> , Christopher A.-L. Jackson<sup>3</sup> , Rebecca E. Bell<sup>1</sup> , and Atle Rotevatn<sup>2</sup> 

<sup>1</sup>Basins Research Group (BRG), Department of Earth Science & Engineering, Imperial College, Prince Consort Road, London, UK, <sup>2</sup>Department of Earth Science, University of Bergen, Bergen, Norway, <sup>3</sup>Department of Earth and Environmental Sciences, University of Manchester, Manchester, UK

**Abstract** Understanding how normal faults grow is key to determining the tectono-stratigraphic evolution of rifts. According to recent studies, normal faults tend to grow in two temporally distinct stages: a lengthening stage, followed by a throw/displacement accumulation stage. However, this model is still debated and not widely supported by many additional studies. Relatively few studies have investigated what happens to a fault as it becomes inactive, that is, does it abruptly die, or does the at-surface trace-length progressively shorten by so-called tip retreat? We, here, use a 3D seismic reflection data set from the Exmouth Plateau, offshore Australia, to develop a three-stage fault growth model for seven normal faults of various sizes and to show how the throw-length scaling relationship changes as a fault dies. We show that during the lengthening stage, which lasted <30% of the faults' lives, faults reached their near-maximum lengths, yet accumulated only 10%–20% of their total throw. During the throw/displacement accumulation stage, which accounts for c. 30%–75% of the faults' lives, throw continued to accumulate along the entire length of the faults. All of the studied faults also underwent a stage of lateral tip-retreat (last c. 25% of the faults' lives), where the active at-surface trace-length decreased by up to 25%. The results of our study may have broader implications for fault growth models, slip rate variability during fault growth, and the way in which faults die, in particular the role of lateral tip-retreat.

### 1. Introduction

Normal fault growth models have been widely debated over the past c. 20 years. The propagating fault model, also referred to as the isolated fault model (Walsh et al., 2003), suggests that normal faults grow via a synchronous increase in length and displacement, that is, that when faults lengthen, they also accumulate displacement. Faults can also lengthen via tip propagation and linkage of these individual segments (e.g., Cartwright et al., 1995; Dawers et al., 1993; Morley et al., 1990; Walsh et al., 2003; Walsh & Watters, 1988). The constant-length model instead suggests that normal faults reach their near-final lengths relatively rapidly and spend the rest of their lives accruing displacement without further significant lengthening (Childs et al., 2017; Fossen & Rotevatn, 2016; Hemelsdaël & Ford, 2016; Henstra et al., 2015; Jackson & Rotevatn, 2013; Nicol et al., 2016, 2005; Tvedt et al., 2016; Walsh et al., 2002, 2003; see also Cowie & Ship-ton, 1998). More recently, Jackson et al. (2017) and Rotevatn et al. (2019) used 3D seismic reflection data and physical analog models to propose a third model, the so-called the “hybrid growth model.” This model states that the propagating fault model and the constant-length models may not in fact be mutually exclusive, end-member models, but instead represent discrete kinematic phases in the life of a single fault: that is, an initial lengthening stage (propagating fault stage) is followed by a later displacement accumulation stage (constant-length stage) (Jackson et al., 2017; Rotevatn et al., 2019). During the lengthening stage, which encompasses c. 20%–30% of the duration of a fault's life, faults reach their near-final length via the propagation and linkage of relatively small, discrete segments; during this time, the fault accumulates 10%–60% of its total displacement (Jackson et al., 2017; Rotevatn et al., 2019). During the displacement accrual stage, which takes place during the latter 70%–80% of the fault's life, the fault accumulates 40%–90% of its total displacement (Jackson et al., 2017; Rotevatn et al., 2019).

Whereas many studies have investigated how normal faults initiate and grow (see above), few have considered what happens at the end of a fault's life. These few studies propose that faults die in two general ways: the entire trace-length of the fault remains active before slip ceases, or that as the fault dies, activity is focused onto the center of the fault, leading to a progressively shorter active fault trace-length (Childs

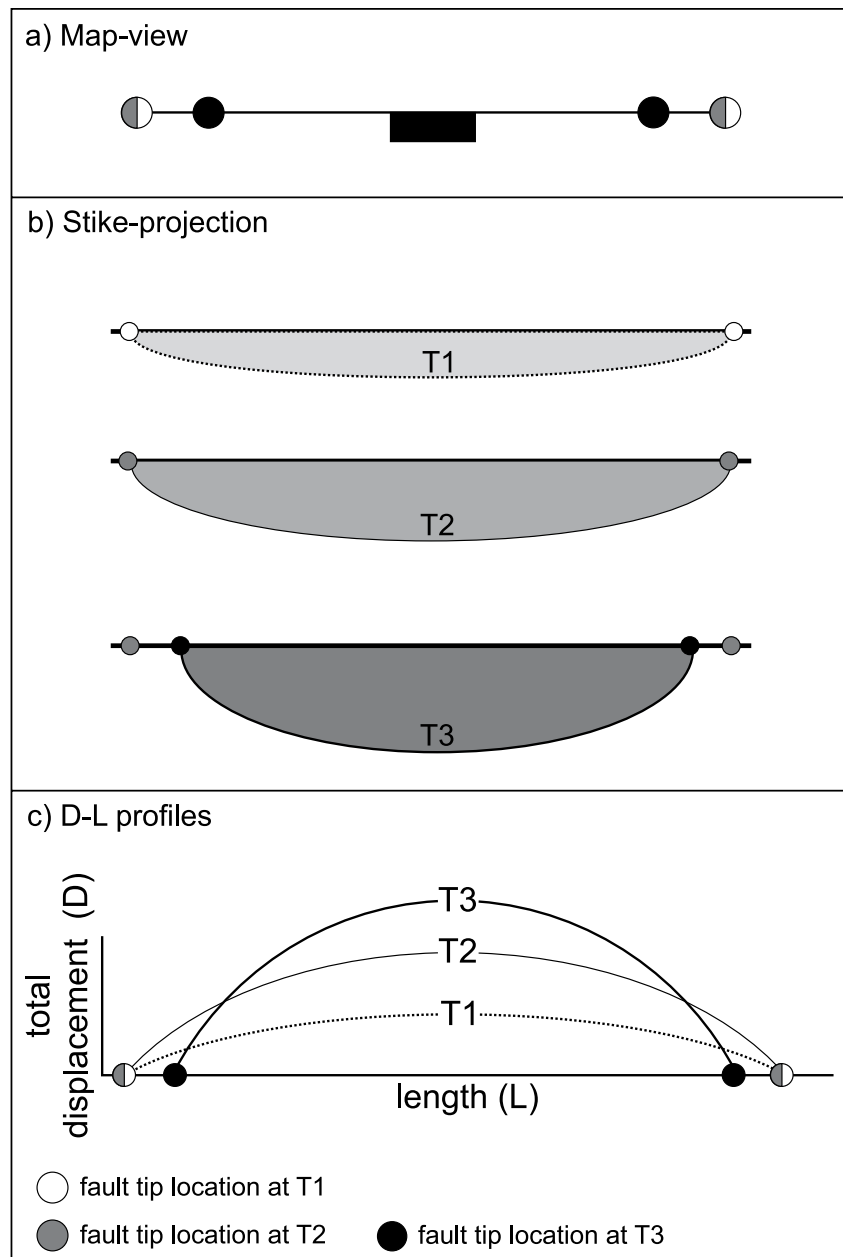


**Figure 1.** Conceptual models for the development of normal faults following a “hybrid fault model” (Rotevatn et al., 2019) with a stage of tip retreat. Time 1 (T1) represents the lengthening/propagating fault model stage, Time 2 (T2) represents the displacement accumulation/constant-length model stage, and Time 3 (T3) represents a phase of fault tip-line retreat. (a) map view of the active fault trace line at T1-3. Note that the fault reaches its maximum length at T1, and has a shorted active trace line at T3. (b) Along-strike projection of throw at T1-3. An increasing amount of displacement is accumulated at each stage. (c) Displacement/length profile at T1-3.

et al., 2003; Meyer et al., 2002). In the latter case, normal faults experience a stage of fault tip retreat, that is, the lateral tip regions do not accumulate further displacement or throw as strain is localized near the fault center (Figure 1; Meyer et al., 2002). In 3D seismic reflection data, tip retreat can be observed by identifying packages of growth strata that are deposited over progressively shorter along-strike lengths as the fault reaches the end of its life (Meyer et al., 2002). Tip retreat has also been interpreted as a result of relay breaching during segment linkage (Childs et al., 2003); however, this is what we would classify as a stage of fault *growth* and not, strictly speaking, lateral tip retreat.

Relatively few studies have discussed the role tip retreat plays in the evolution of normal faults (Childs et al., 2003; Freitag et al., 2017; Meyer et al., 2002; Morley, 2002; Nicol et al., 2020), and it is therefore not usually included in fault growth models. This likely reflects the fact it is very difficult or sometimes impossible to constrain the kinematics of normal faults, for example in cases where growth strata are absent and/or only locally preserved. To the best of our knowledge, tip retreat has also not yet been the focus of or identified in, physical or numerical models. Freitag et al. (2017) show an example of tip retreat in the Columbus Basin, offshore Trinidad; these are, however, thin-skinned, gravity-driven faults, and it is not clear if the kinematics would apply to thick-skinned faults offsetting crystalline basement. Morley (2002) also show an example of possible tip retreat in the East African Rift, but since this is a sediment-starved (i.e., underfilled) basin, it is difficult to tell if the fault really experienced tip retreat, or whether the observed geometries simply reflect post-fault death passive filling of hanging wall accommodation. Motivated by the lack of examples that highlight the potentially important role of tip retreat, we here provide a well-constrained example of tip retreat occurring on basement-involved, tectonically (i.e., plate-motion) driven normal faults, as well as guidance on how to identify this important process in the rock record.

In this paper, we use 3D seismic reflection and borehole data from the Exmouth Plateau, offshore Australia to study the kinematics of thick-skinned tectonic normal faults that offset crystalline basement. More specifically we: (1) constrain the temporal relationship between fault lengthening and throw and (2) investigate the role of tip retreat as faults become inactive. This is an excellent place to study this process because synsedimentary normal faults are well-preserved, age-constrained, and well-imaged in excellent-quality, open-source, 3D seismic reflection data. The rift basin was also overfilled for much of the duration of faulting, meaning the faults are flanked by well-developed growth (syn-tectonic) strata.

## 2. Geologic Setting of the Exmouth Plateau

Our study area is located on the Exmouth Plateau, North Carnarvon Basin, offshore NW Australia (Figure 2). The North Carnarvon Basin formed due to rifting in the Late Carboniferous-Permian as a result of the breakup of Pangea, and the Exmouth Plateau formed as a result of rifting between Greater India and Australia, creating NE-trending blocks (Gibbons et al., 2012; Longley et al., 2002; Stagg & Colwell, 1994). The Exmouth Plateau is located in the northern part of the North Carnarvon Basin, bounded by the continental shelf to the southeast, and the Curvier, Gascoyne, and Argo abyssal plains to the SW, SW, and NE, respectively (Longley et al., 2002). The Exmouth Plateau is a block of thin crystalline crust, and based on geophysical evidence, it has been suggested that the Exmouth Plateau basement is continental crust, however this has not been confirmed by direct sampling (Stagg et al., 2004). The crystalline basement is overlain by a thick pre-rift succession, consisting of the fluvial-deltaic to marginal marine, Mungaroo Formation (Triassic) (Longley et al., 2002; Stagg et al., 2004).

The synrift extension began in the Late Triassic (Rhetian) until Late Jurassic (Oxfordian), during which time the Murat and Athnol siltstones were deposited in a sediment-starved basin (Figure 3) (Longley et al., 2002; Tindale et al., 1998). After a short period of tectonic quiescence in the Late Jurassic, rifting continued in the Early Cretaceous in an over-filled basin environment, during which time marine claystones (Dingo Claystone) and coarser-grained, deltaic clastics (Barrow Group) were deposited (Longley et al., 2002). Rifting in the Exmouth Plateau ceased in the Hauterivian, and the area became a passive margin (Gibbons et al., 2012; Longley et al., 2002). In this paper, we focus on the Jurassic-Early Cretaceous, syn-sedimentary normal faults which are generally trending N-NE.

## 3. Data

### 3.1. Data

The Glencoe data set is a 3D time-migrated seismic reflection survey that encompasses approximately 3,900 km<sup>2</sup> of the Kangaroo syncline in the Exmouth Plateau (Figure 4). It has a bin spacing of 25 m and a record length of 8 s two-way time (TWT). The vertical and horizontal resolution are approximated by measuring the dominant wavelength in the interval of interest ( $\lambda = 26.3$  m) and calculating  $\lambda/4$  (where  $\lambda$  is the seismic wavelength), yielding c. 6.6 m within the syn-rift sequence (Brown, 2011).

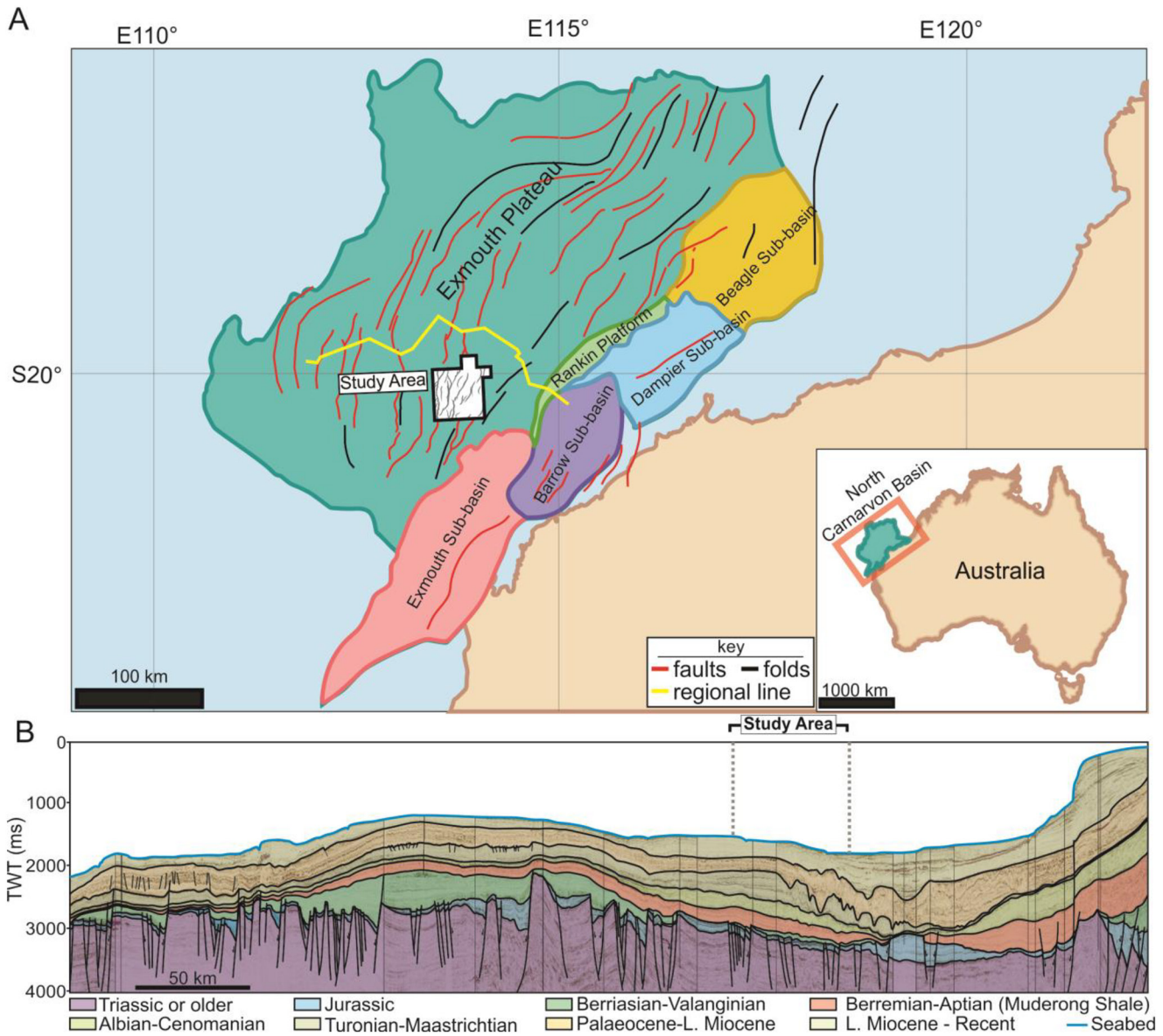


**Figure 2.** Study area. (a) Location of the Exmouth Plateau in the North Carnarvon Basin, offshore Australia (fault locations modified from Pan et al., 2020), (b) Regional 2D seismic line across the study area, modified from Nugraha et al. (2019). The location of this regional line is labeled on Figure 2a (yellow).

Seismic sections are displayed with normal polarity (SEG European Convention; Brown, 2011), where increase in acoustic impedance is represented by a peak (red), and a decrease by a trough (black). Seismic in-lines are orientated WNW-ESE and the survey is tied to four wells (Glencoe-1, Nimblefoot-1, Warrior-1, and Breseis-1). Well-logs, formation tops, and biostratigraphic ages were provided with the wells. All seismic and well data are open-access and available from Geoscience Australia.

We have mapped seven regionally extensive seismic horizons (H1-7); H1, H5, H6, and H7 are age-constrained well-tied horizons with ages from well reports, as well as ages obtained by Marshall and Lang (2013) using biostratigraphy from 1,500 wells around the North Carnarvon Basin (Figure 3). We lack direct age-constraints for H2-4, thus we estimated their ages by assuming a constant sedimentation rate between horizons of known ages (Figure 3). We also locally picked additional horizons within the syn-sedimentary deposits (e.g., H5.5) that are not continuous across the entire data set; we estimated their ages based on an assumption of constant sedimentation rates between overlying and underlying, age-constrained horizons. We mapped and analyzed seven faults of varying sizes (8.8–42 km long, with 165–680 m of throw) to show

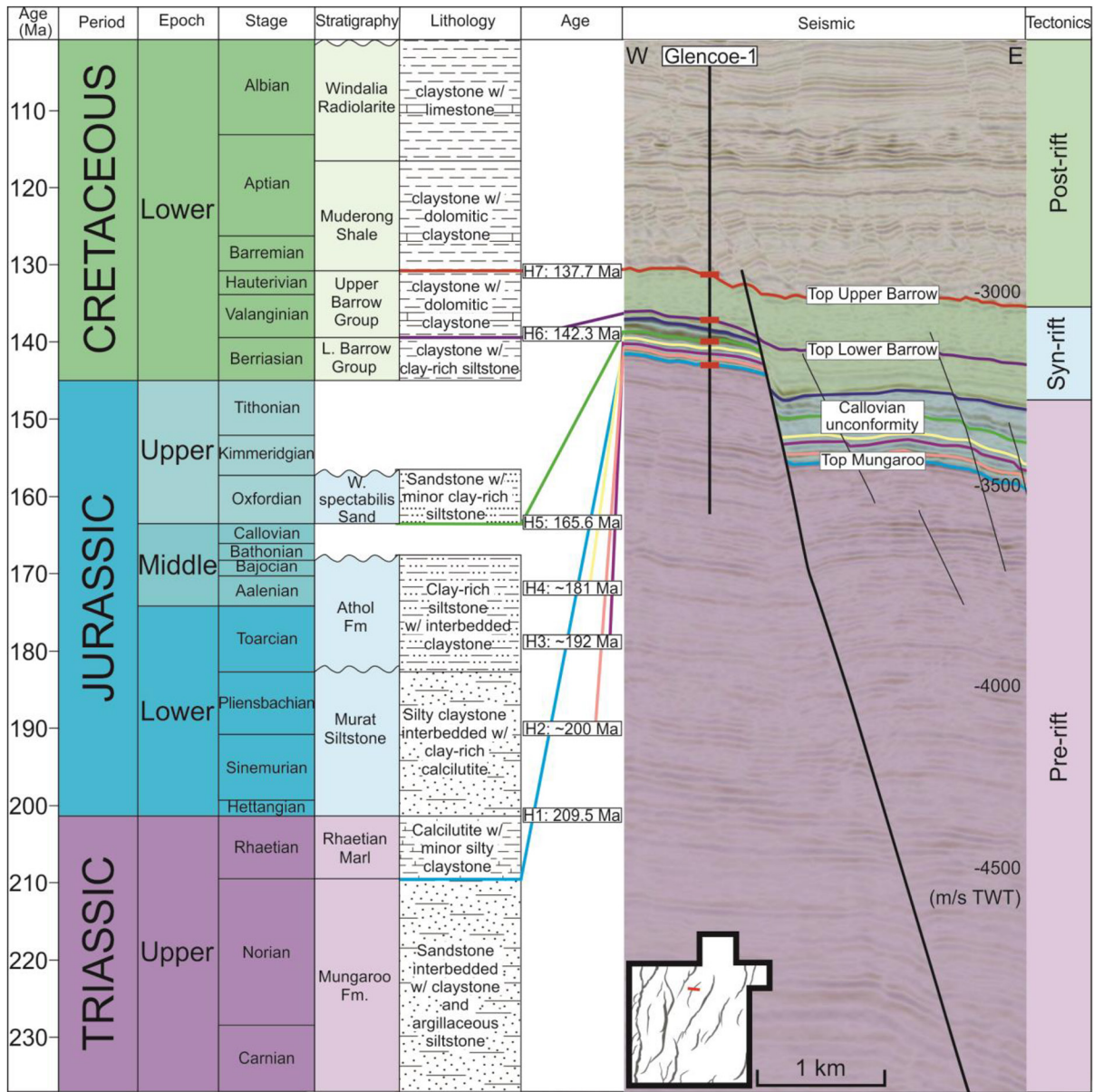


**Figure 3.** Stratigraphic framework showing the key interpreted seismic horizons, their ages, and the tectonic evolution of the Exmouth Plateau (H = horizon). Ages for H1, H5, H6, and H7 were taken from Marshal and Lang (2013), and H2, H3, and H4 are relative dates assuming constant sedimentation. Information on the tectonostratigraphic framework are from Bilal et al. (2018) and Geoscience Australia.

how faults of different sizes grow in the area, and to see if the styles of fault growth are scale dependent (see Figure 5 for fault locations).

### 3.2. Methodology

In this study we used three different methods to quantify fault growth: isochron analysis, throw backstripping, and expansion index (EI) analysis (see review by Jackson et al., 2017). First, we created time-thickness (isochron) maps of key stratigraphic intervals, which illustrate variations in sediment thickness. This highlights across-fault hanging wall thickening, which can reveal the growth history of a fault (e.g., Jackson & Rotevatn, 2013). Isochron analysis was done first in order to establish the general style of fault growth (i.e., a propagating, constant-length, or hybrid fault growth model), and then we conducted throw backstripping to be able to see exact fault throw and length through time in the faults' lives (Jackson et al., 2017). To

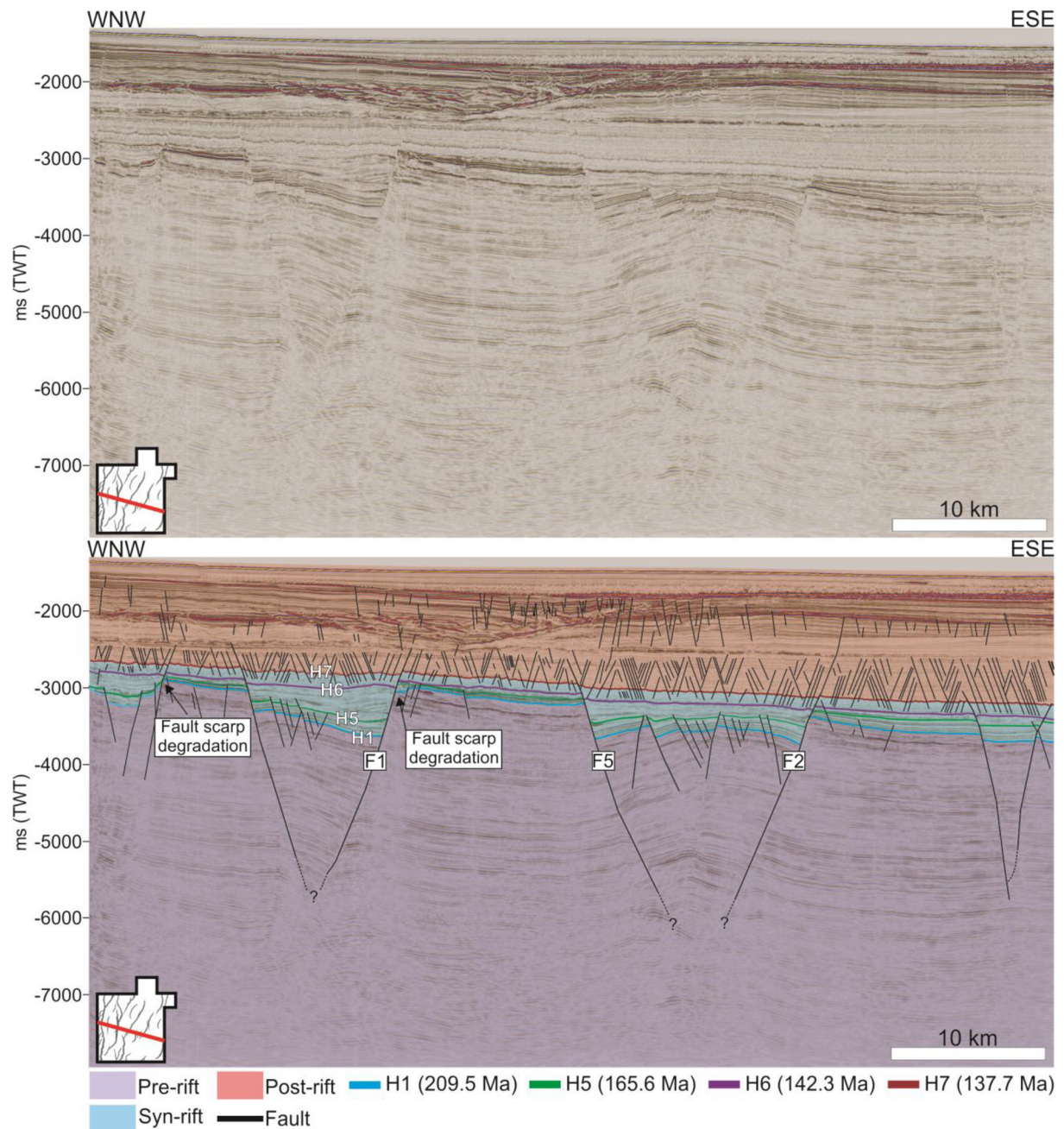


**Figure 4.** Representative seismic line in TWT along the central section of the 3D data set, across strike of the studied faults. Data is shown with and without interpretation.

begin throw backstripping, we created throw-length (T-x) plots by picking the hanging wall and footwall cutoffs for every chosen horizon across the length of the faults (appendix Figures A1–A3). In the case of folding or erosion (Figure 4), horizons used to calculate throw were projected across the fold or eroded fault scarp (e.g., Wilson et al., 2013). Throw backstripping involves subtracting the throw of a shallower horizon directly from the throw of a deeper horizon at the same along-strike position, with this being repeated for successively deeper horizons (Chapman & Meneilly, 1991; Peterson et al., 1992). We opted to use the “original method” of throw backstripping, where throw across different horizons is simply subtracted, as we did not want to make any assumptions about the style of fault growth (see Jackson et al., 2017 for more details on fault displacement backstripping methods). Finally, we used EI analysis to measure variations in stratal

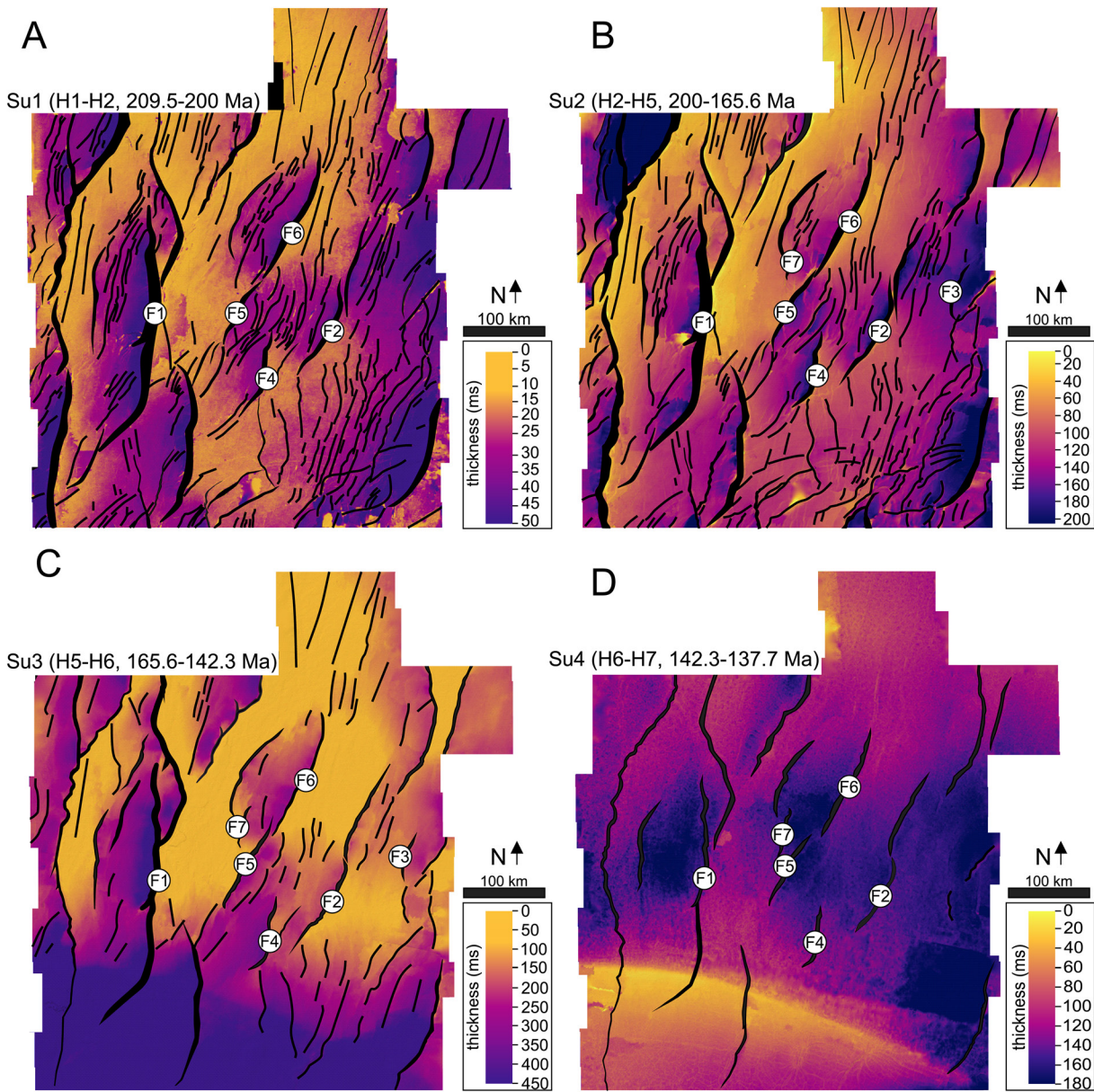


**Figure 5.** Representative isochrons of the study area with interpreted major and minor faults labeled. (a) Seismic Unit 1: Horizon 1–2, 209.5–200 Ma, (b) Seismic Unit 2: Horizon 2–5, 200–165.6 Ma, (c) Seismic Unit 3, Horizon 5–6. 165.6–142.3 Ma, (d) Seismic Unit 4, Horizon 6–7. 142.3–137.7 Ma.

thickness across the fault by dividing the thickness of hanging wall stratal unit by that of the equivalent unit in the footwall (Bouroullec et al., 2004; Cartwright et al., 1998; Jackson et al., 2017; Thorsen, 1963) (See appendix Figure A4). This technique shows the formation and growth of depocenters, and therefore how the faults lengthened (Jackson & Rotevatn, 2013).

We also calculated vertical throw gradients by dividing the change in throw by the change in depth of the shallowest two horizons offset across the fault. We calculated upper-tip throw gradients in order to demonstrate that the top of the fault was interacting with the free surface rather than acting as a blind fault; this is important when trying to understand if faults experienced real tip-line retreat or not (Childs et al., 2003; Meyer et al., 2002; Walsh & Watterson, 1988). Finally, we calculated fault slip rates by dividing displacement for a particular time period by the duration of that time period; this was done in order to investigate whether slip rates varied between the different stages of fault growth. It is important to note that we plotted total throw and length through time using data derived from: (i) all seven of our seismic-stratigraphically defined

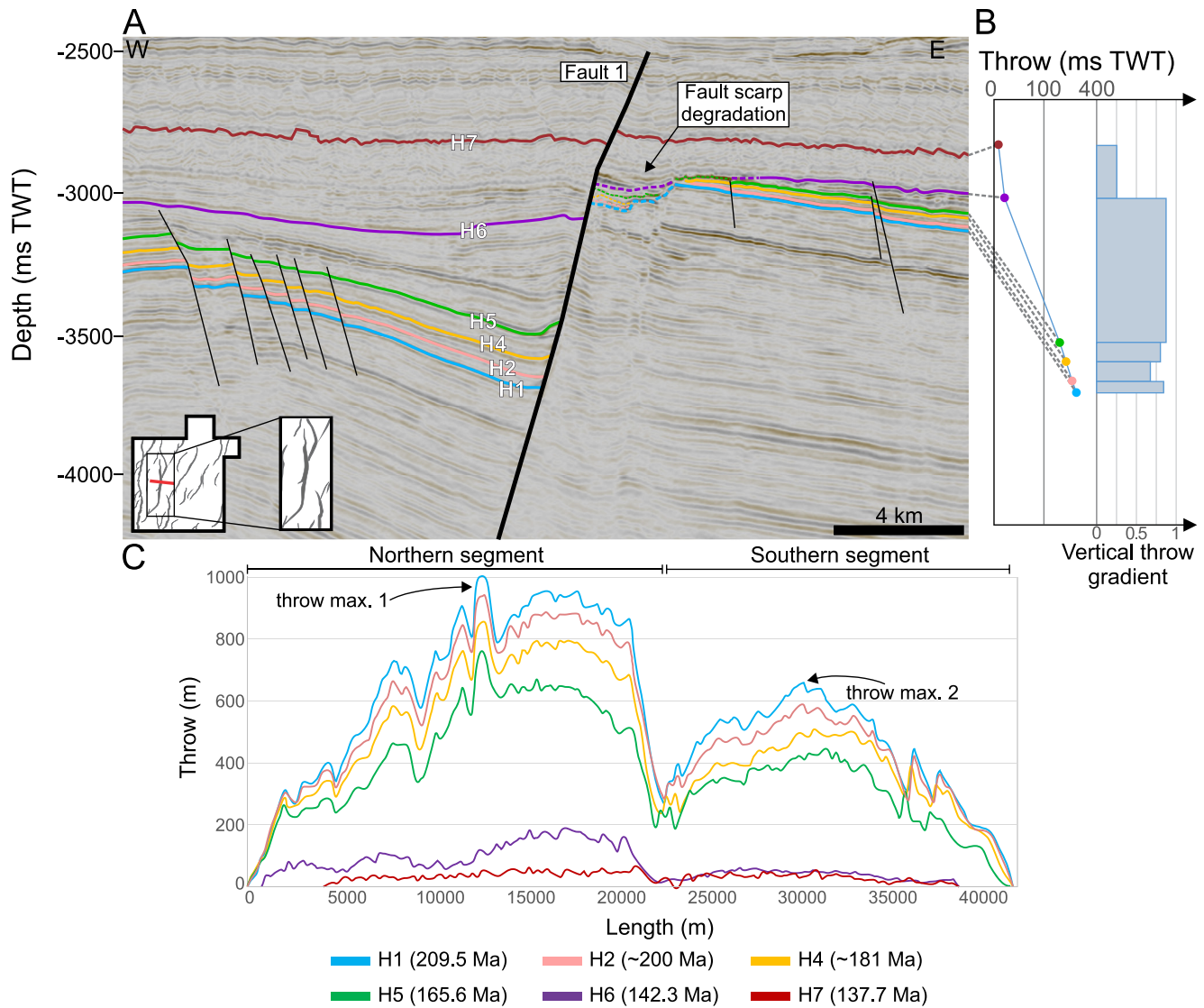


**Figure 6.** (a) Seismic profile illustrating F1 at its point of highest throw and its correlated throws and throw gradients, (b) Vertical throw gradients for each horizon, (c) Throw-distance plot illustrating the lateral variations in throw across each seismic unit. All throw values could be underestimated up to 20% due to post-depositional compaction of faulted strata (Taylor et al., 2008).

horizons, four of which were directly age-constrained by well data, and three for which the ages were only estimated (see above); and; (ii) only our four age-constrained seismic horizons. We plotted slip rate through time using only age-constrained horizons. This allowed us to constrain a range of rates for time-variable parameters, which future additional well data may help refine.

Since the basin was sediment-starved from the Early Jurassic until the Late Jurassic, as evidenced by the fault scarp degradation until the deposition of H5 (Figures 4, 6a, and 8a), our fault lengthening calculations are upper limit estimations. For example, if active faulting created hanging wall accommodation but the basin was sediment starved, this accommodation would have remained unfilled. Thus, what looks like tip propagation could just be prolonged filling of the hanging wall of an inactive normal fault (see Jackson et al., 2017). It is therefore possible that the faults reached their maximum lengths even quicker than what we estimate.

There is a level of uncertainty when attempting to map fault tip positions in 3D seismic, even with high-quality data (Pickering et al., 1996). Our seismic data set has a vertical and horizontal resolution of c. 6.6 m; this means faults smaller (i.e., shorter and with less displacement) than this value are not imaged, and that the



tips of otherwise larger faults will also not be imaged. Because of this, it is likely we are underestimating fault lengths by a few hundred meters (see Pickering et al., 1996). However, this seismic imaging resolution issue applies at all stages of fault growth and therefore does not impact our key observations (i.e., that EI values fall below 1 near the fault tips during the later stages of their lives) and related interpretations (i.e., that the active fault-trace length shortens as the fault dies).

We use checkshot (velocity) data from our four wells to convert throw values from milliseconds two-way time (m s TWT) to depth (m) (see appendix Figure A1). Throw values are presented in meters. Burial-related compaction of sedimentary rocks can result in throw calculations being underestimated, especially when rocks have a high shale content or are deeply buried (>2 km; see Taylor et al., 2008). Decompaction typically decreases throw estimates by <20% (Taylor et al., 2008), so we here give all throw and slip rate values an error to account for maximum of 20% decompaction.

## 4. Results

We have completed a comprehensive geometric and kinematic analysis of seven faults of various sizes (appendix Figures A2–A7). We first provide a detailed description of the geometry of three faults (and their related growth strata) that are representative of the various fault sizes identified in the study area, before describing their kinematics. Fault 1 (F1) represents the largest studied fault, Fault 2 (F2) represents a mid-sized fault, and Fault 3 (F3) represents the smallest studied fault in the data set. We then present and discuss the results for all of the studied faults.

### 4.1. Fault 1

#### 4.1.1. Observations

Fault 1 (F1), the largest fault in the data set that has both of its tips imaged, is ~42 km long, strikes N-S, and dips to the E. Based on along-strike changes in strike and throw (Figure 6c), we split F1 into a 24 km-long northern segment and an ~18 km-long southern segment (Figures 5 and 6). The upper tip-line of F1 is located in Lower Cretaceous strata, where it physically links to a tier of polygonal faults (Velayatham et al., 2019) (Figure 4), and its lower tip-line is difficult to locate due to poor seismic imaging in the pre-rift, but F1 appears to tip out deep in the study area or into the basement (Figure 4). F1 shows two clear throw maxima; a northern maximum (680 + 136 m s TWT or 1,000 + 200 m at H1; error shows possible decompaction) near the center of the northern fault segment, and a southern maximum (433 + 87 m s TWT, 658 + 132 m at H1) near the center of the southern fault segment. Both segments are generally characterized by approximately bell-shaped throw distributions, the peak of which is skewed away from the center due to the related throw maxima being offset from the fault segment center (Figure 6c).

There are clear wedge-shaped stratigraphic packages between H1 and H7 in the hanging wall; these thicken toward F1. In contrast, pre-H1 and post-H7 strata are isopachous (Figure 6a). EI plots show across-fault thickening (i.e., values  $\geq 1$ ) in Unit 1 along the central parts of the northern and southern segments; the unit is, however, isopachous where the two segments link (Figure 7a). In contrast, EI values in Unit 2 are  $\geq 1$  across the link between the two segments (Figure 7b). EI values are  $\geq 1$  across a progressively longer portion of the fault in Units 2–5 (Figures 7b–7d), until the youngest interval, Unit 6 (Figure 7e), where the upper tip of the fault is associated with EI values <1.

#### 4.1.2. Interpretations

We see across-fault thickening in the hanging wall between H1 and H7 (Units 1–5) in cross section (Figure 6a) and in isochron thickness maps (Figures 7a–7e), suggesting F1 was active from 209.5 to 137.7 Ma (Early Jurassic–Early Cretaceous). In detail, however, the EI plots show that different parts of the fault were active at different times. The fact that F1 is associated with two discrete throw maxima (and two associated bell-shaped throw distributions), as well as an EI of <1 in the middle of the fault in the first time interval (Unit 1; Figure 7a), suggests it formed by the linkage of two, initially separate segments. Linkage likely occurred sometime between the deposition of H2 and H4, based on EI values of >1 only occurring in units above H1. Often, when faults link, their paleo-tip-lines become inactive (Childs et al., 2003). In this case, however, F1 is a footwall-breached relay and the tip of the northern segment continued to accrue

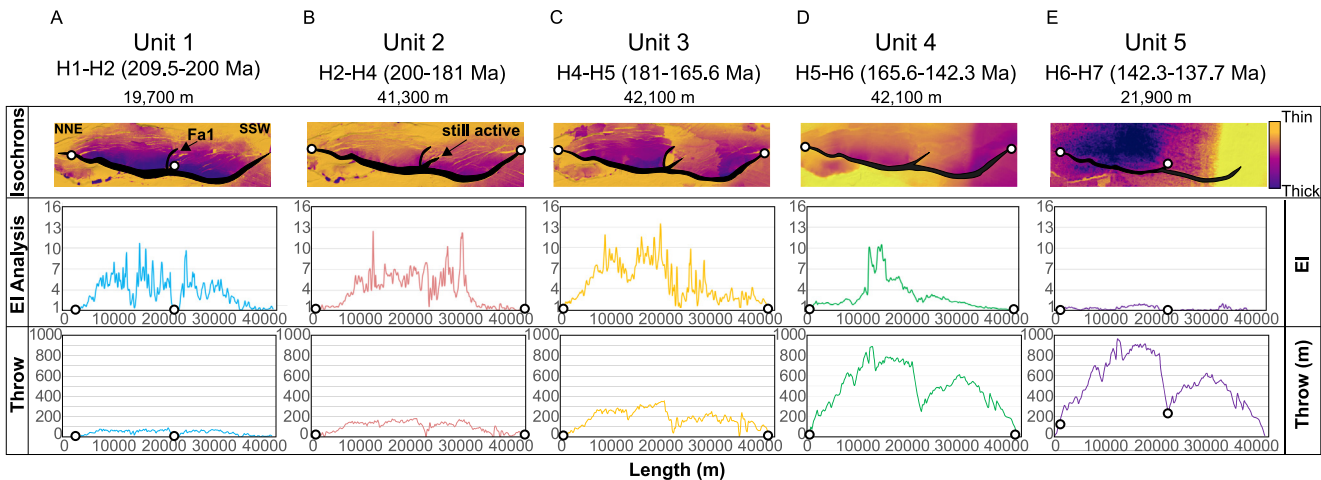


**Figure 7.** Isochrons, expansion index analysis, and throw throughout different stages of the life of F1. The throw through time values are taken from throw backstripping, which can be seen in detail in the appendix figures. White dots indicate the length of the fault at the specified interval. (a) Isochron showing the thickness between H1 (209.5 Ma) and H2 (200 Ma), maximum throw is 78 m, and length is 19,700 m, (b) Isochron showing the thickness between H2 (200 Ma) and H4 (181 Ma), maximum throw is 191 m and length is 41,300 m, (c) Isochron showing the thickness between H4 (181 Ma) and H5 (165.6 Ma), maximum throw is 438 m and length is 41,100, (d) Isochron showing the thickness between H5 (165.6 Ma) and H6 (142.3 Ma), maximum throw is 993 m and length is 42,100, (e) Isochron showing the thickness between H6 (142.3 Ma) and H7 (137.7 Ma), maximum throw is 1,098 and length is 21,900 m. All throw values could be underestimated up to 20% due to post-depositional compaction of faulted strata (Taylor et al., 2008).

displacement on portions of the fault tips bounding the now-breached relay ramp (Figure 7e). The lack of throw in the middle of the fault is likely due to the still-active northern segment paleo-fault tip accommodating strain in the middle of the fault, as well as a minor E-W fault (labeled F1a in Figure 7a) that cuts perpendicularly across F1. F1 reached its maximum length by the deposition of H5 (Unit 3), or possibly sooner, based on the observation of EI values  $\geq 1$  across its length for this interval (Figure 7c). During Unit 5, the lateral ends of the fault have an EI value of  $< 1$ , which suggests that the fault tips became inactive at this time. Additionally, during this last stage of fault growth, the breached relay ramp between the northern and southern segment had an EI value of  $< 1$ , which suggests that the fault along the previously active relay ramp between the two fault segments became inactive (Figure 6e).

In summary, according to throw backstripping and EI analysis, F1 initiated after the deposition of H1 (c. 209.5 Ma), and within c. 9.4 Myr (13% of its total life) consisted of two separate segments that were 19.7 and 19.2 km long. During this first phase of activity, it accumulated only 7% of its total throw. Approximately 18.8 Myr later, the two segments linked and the outermost tips of the newly formed fault system had propagated slightly, meaning it was now 41.3 km long. The fault had therefore reached c. 98% of its maximum length and accrued 19% of its total throw by this point (i.e., 39% of its life). Its maximum length was reached 15.7 Myr later, by which time it had accumulated 36% of its total throw. During the last 4.6 Myr of the fault's life, the remaining throw was accrued, and the northernmost 0.9 km and southernmost 2.9 km became inactive.

## 4.2. Fault 2

### 4.2.1. Observations

Fault 2 (F2) is a 19 km long, NNE-SSW-striking, WNW-dipping normal fault. F2 comprises a long (11 km) central segment that is linked at each end via abrupt bends, to shorter (3–5 km) segments (Figures 8 and 9). The upper tip-line of F2 is located in Lower Cretaceous strata, and its lower tip-line is difficult to locate due to poor seismic imaging in the pre-rift, but F2 appears to tip out deep in the study area or into the basement (Figure 4). F2 presently has three local throw maxima; a central maxima (380 + 76 m s TWT, 620 + 124 m at H1) on the main, central segment, a southern maxima (348 + 70 m s TWT, 560 + 112 m at H1) that is located along the southern fault segment, and a smaller, northern maxima (94 + 19 m s TWT, 150 + 30 m at H1) on the northern fault segment (Figure 8b). The throw maxima are separated by two throw minima

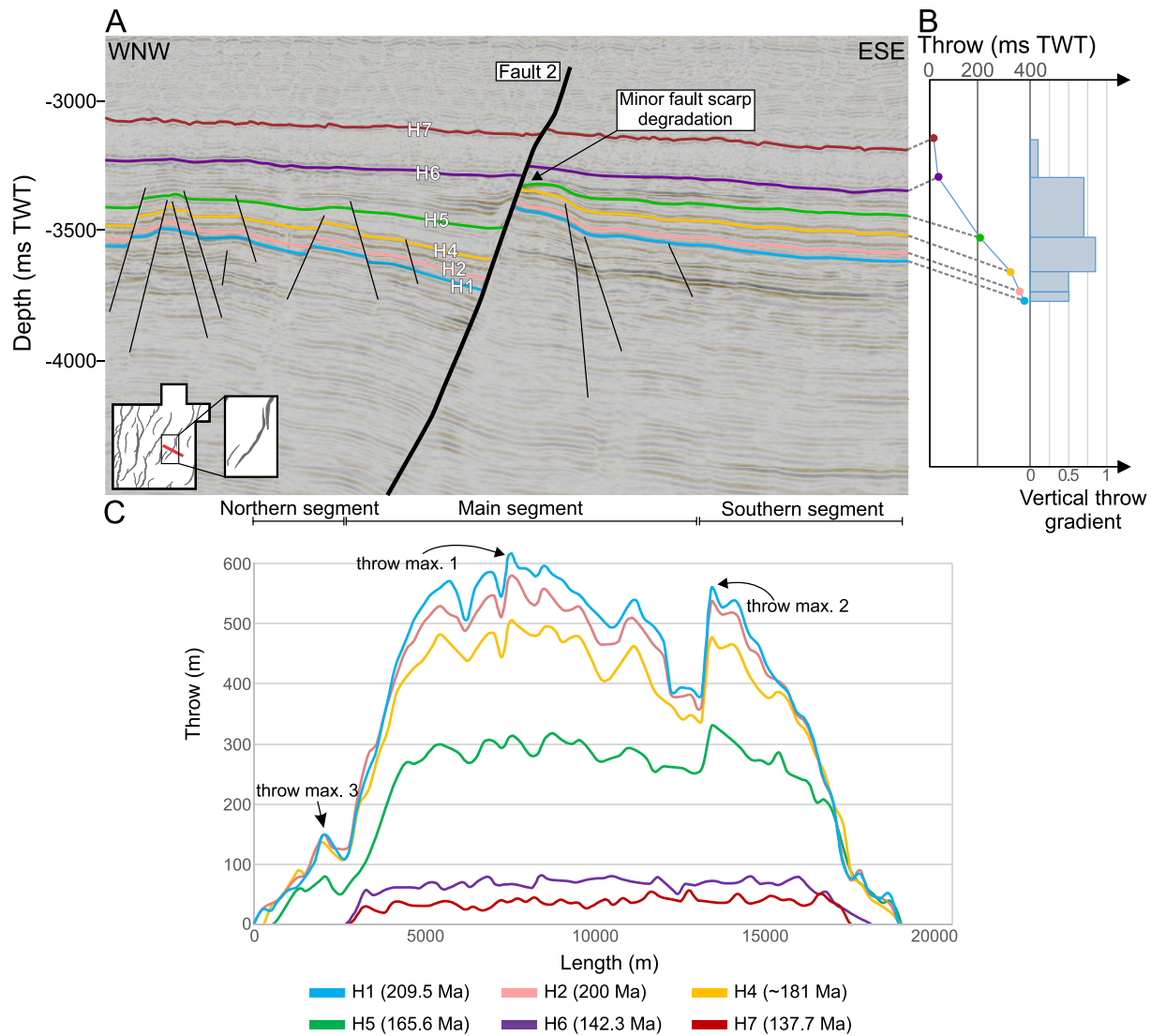


**Figure 8.** (a) Seismic profile illustrating F2 at its point of highest throw and its correlated throws and throw gradients, (b) Vertical throw gradients for each horizon, (c) Throw-distance plot illustrating the lateral variations in throw across each seismic unit. All throw values could be underestimated up to 20% due to post-depositional compaction of faulted strata (Taylor et al., 2008).

that coincide with the abrupt bends in the map-view trace of F2, where the northern and southern segments connect with the central segment (Figure 9). The main segment has an overall symmetrical throw distribution, and the northern and southern segments are skewed to the south and north respectively (Figure 8b).

There are clear wedge-shaped stratigraphic packages between H1 and H7 in the hanging wall, which thicken toward F2. Pre-H1 and post-H7 strata are isopachous (Figure 8a). EI plots show values  $\geq 1$  along a progressively longer portion of the fault from the oldest to the second youngest stratigraphic intervals (Units 1–4; Figures 9a–9d). In Unit 5, the lateral tips of the fault have an EI value that is  $< 1$  (Figure 9e).

#### 4.2.2. Interpretations

We see across-fault thickening between H1 and H7 (Units 1–5) in cross-section (Figure 8a) and in isochron thickness maps (Figures 9a–9e), suggesting F2 was active from 209.5 to 137.7 Ma (Early Jurassic–Early Cretaceous). The fact that EI values  $\geq 1$  are limited to the central segment of the fault in Unit 1 (Figure 9a) suggests that F2 initiated here, an interpretation that is supported by the symmetry of the throw distribution on this segment (Figure 8b). The shorter southern segment was clearly present and active by Unit 3 (Figure 9c) and possibly already by Unit 2 (Figure 9b) times, as evidenced by EI values  $\geq 1$  along these segments in the

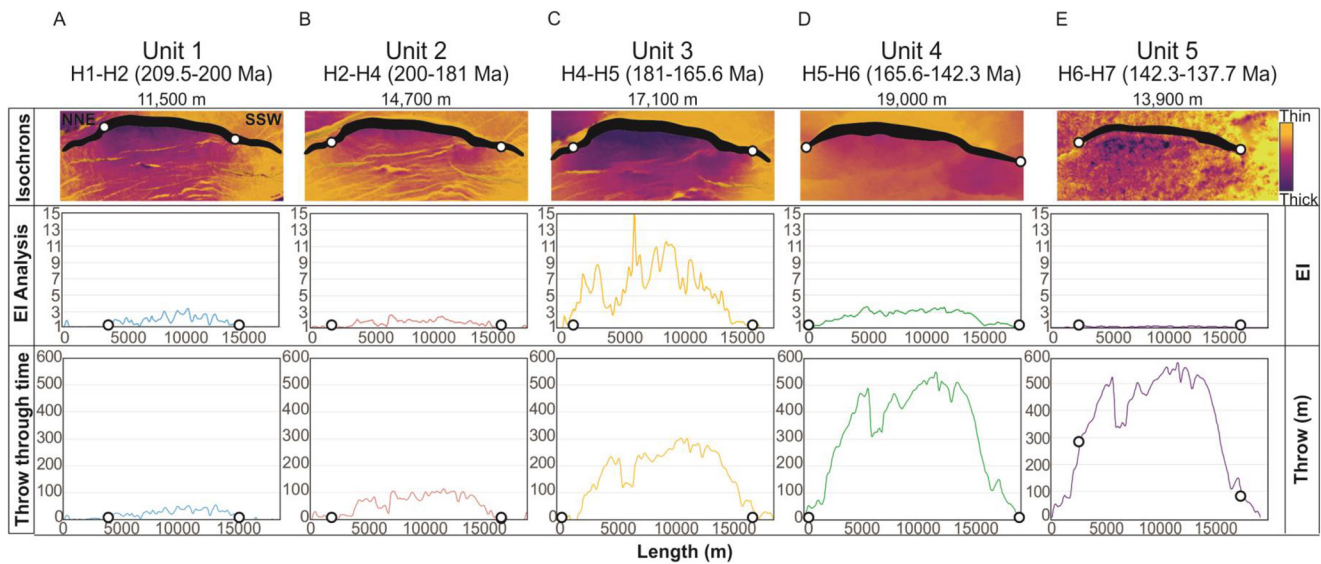


**Figure 9.** Isochrons, expansion index analysis, and throw throughout different stages of the life of F2. The throw through time values are taken from throw backstripping, which can be seen in detail in the appendix figures. White dots indicate the length of the fault at the specified interval. (a) Isochron showing the thickness between H1 (209.5 Ma) and H2 (200 Ma), maximum throw is 55 m, and length is 11,500 m, (b) Isochron showing the thickness between H2 (200 Ma) and H4 (181 Ma), maximum throw is 116 m and length is 14,700 m, (c) Isochron showing the thickness between H4 (181 Ma) and H5 (165.6 Ma), maximum throw is 303 m and length is 17,100, (d) Isochron showing the thickness between H5 (165.6 Ma) and H6 (142.3 Ma), maximum throw is 550 m and length is 19,000, (e) Isochron showing the thickness between H6 (142.3 Ma) and H7 (137.7 Ma), maximum throw is 617 and length is 13,900 m. All throw values could be underestimated up to 20% due to post-depositional compaction of faulted strata (Taylor et al., 2008).

corresponding interval. The throw maxima on the southern segment is skewed toward the NNE (Figure 8b), which is interpreted as a result of the mechanical interaction of the southern section with the already-existing central segment (Wilkinson et al., 2015). The northern segment was present and active by Unit 3 times (c. 28.2 Myr), based on the observation of EI values  $\geq 1$  along the segment (Figure 9c). This northern segment may have simply formed due to lateral (i.e., north-northeastward) propagation of the northern tip of the central segment. However, our preferred interpretation is that it initiated as a separate segment, based on: (i) the observed EI distribution within Unit 4 (i.e., the EI peak is located centrally along the SSW segment; Figure 9c); (ii) the fact the throw maximum is offset to the SW of the center of the mapped trace of the northern segment (Figure 8b); and (iii) the pronounced bend between the central and northern segments, which we infer reflects a now-breached relay ramp (Peacock & Sanderson, 1994; Walsh et al., 1999). F2 reached its maximum length by the deposition of H5, or possibly sooner, as evidenced by EI  $\geq 1$  across its length during this interval. EI values drop below 1 on the lateral tips of F2 in Unit 5, which we interpret as the outer 2–2.5 km of the fault becoming inactive (Figure 9e).

In summary, according to throw backstripping and EI analysis, F2 initiated after the deposition of H1 (c. 209.5 Ma), and within c. 9.4 Myr (13% of its total life) was 11.5 km long (60.5% of maximum length). During this first phase of activity, F2 only accumulated c. 13% of its total throw. Approximately 18.8 Myr later, F2 had grown via tip propagation and possibly segment linkage to be 14.7 km long. At this time, the fault had reached 77.4% of maximum length and only 20% of total throw by this point (39.3% of the fault's life). C. 15.7 Myr later (i.e., 50.2% of the total life), the central segment of F2 grew via segment linkage to be 17.1 km long, and accumulated c. 52.4% of total throw. Its maximum length was reached within the next 23.3 Myr, by which time it had accumulated c. 95.1% of its total throw. During the last 4.6 Myr of the fault's life, the remaining 4.9% of throw was accrued, and the northernmost 2.6 km and southernmost 2.4 km of the fault became inactive.

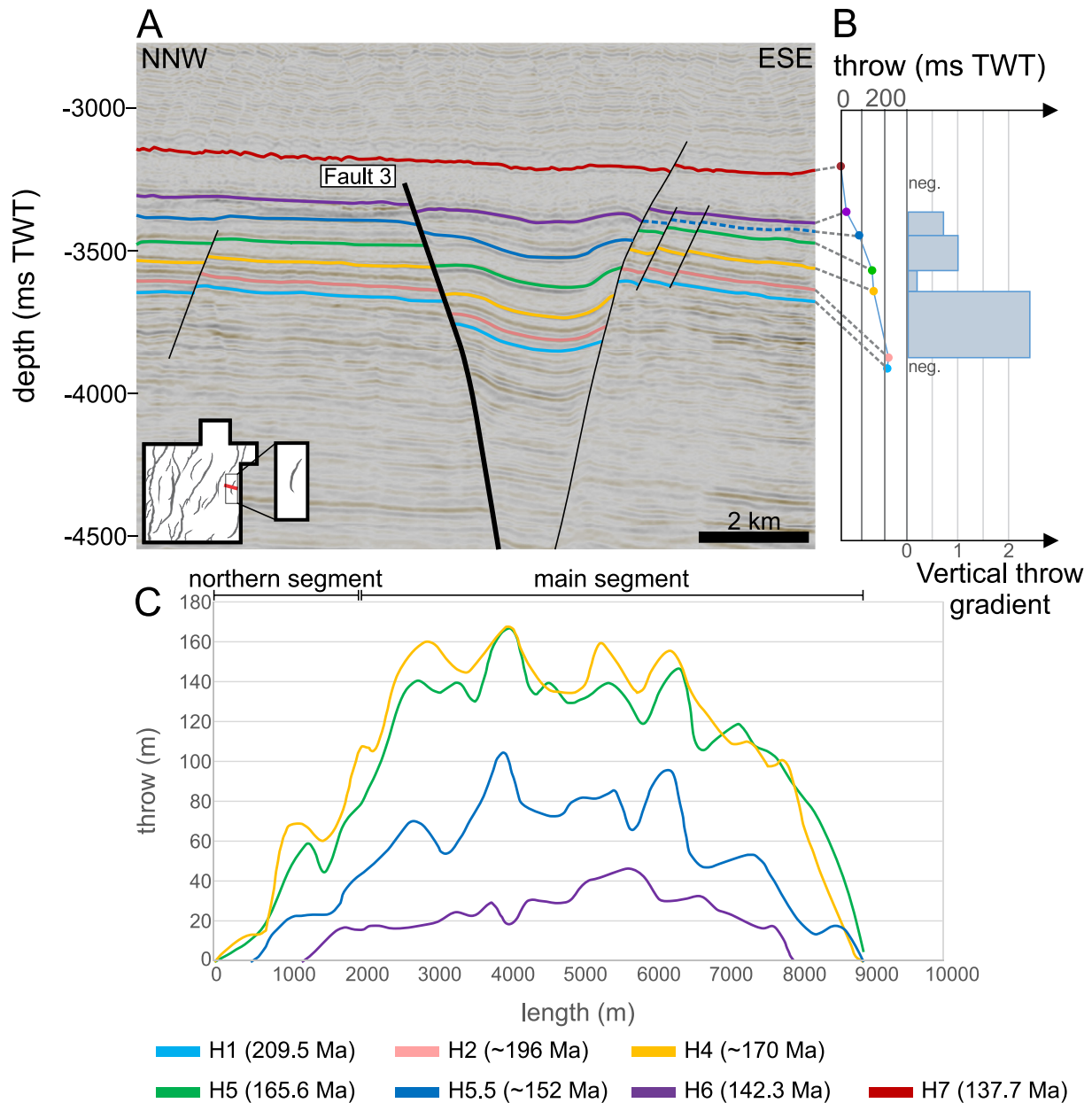


**Figure 10.** (a) Seismic profile illustrating F3 at its point of highest throw and its correlated throws and throw gradients, (b) Vertical throw gradients for each horizon, (c) Throw-distance plot illustrating the lateral variations in throw across each seismic unit. All throw values could be underestimated up to 20% due to post-depositional compaction of faulted strata (Taylor et al., 2008).

### 4.3. Fault 3

#### 4.3.1. Observations

Fault 3 (F3) is an 8.8 km long, NNE-SSW-striking, ESE-dipping normal fault. Its plan-view geometry consists of a slightly curved, convex-into-the-footwall segment with a small (1 km) fault branch near its northern tip (Figures 10 and 11). The upper tip-line of F3 is located in Lower Cretaceous strata, and its lower tip-line is difficult to locate due to poor seismic imaging in the pre-rift, but F3 appears to tip out deep in the study area (Figure 10). The present-day throw distribution for F3 shows two throw maxima; the main maxima (165 + 33 m, 83 + 17 m s TWT at H4) is located in the center of the main segment, with another, more minor maxima (59 + 12 m, 37 + 7 m s TWT at H4) being associated with a possible northern segment (Figure 10b).

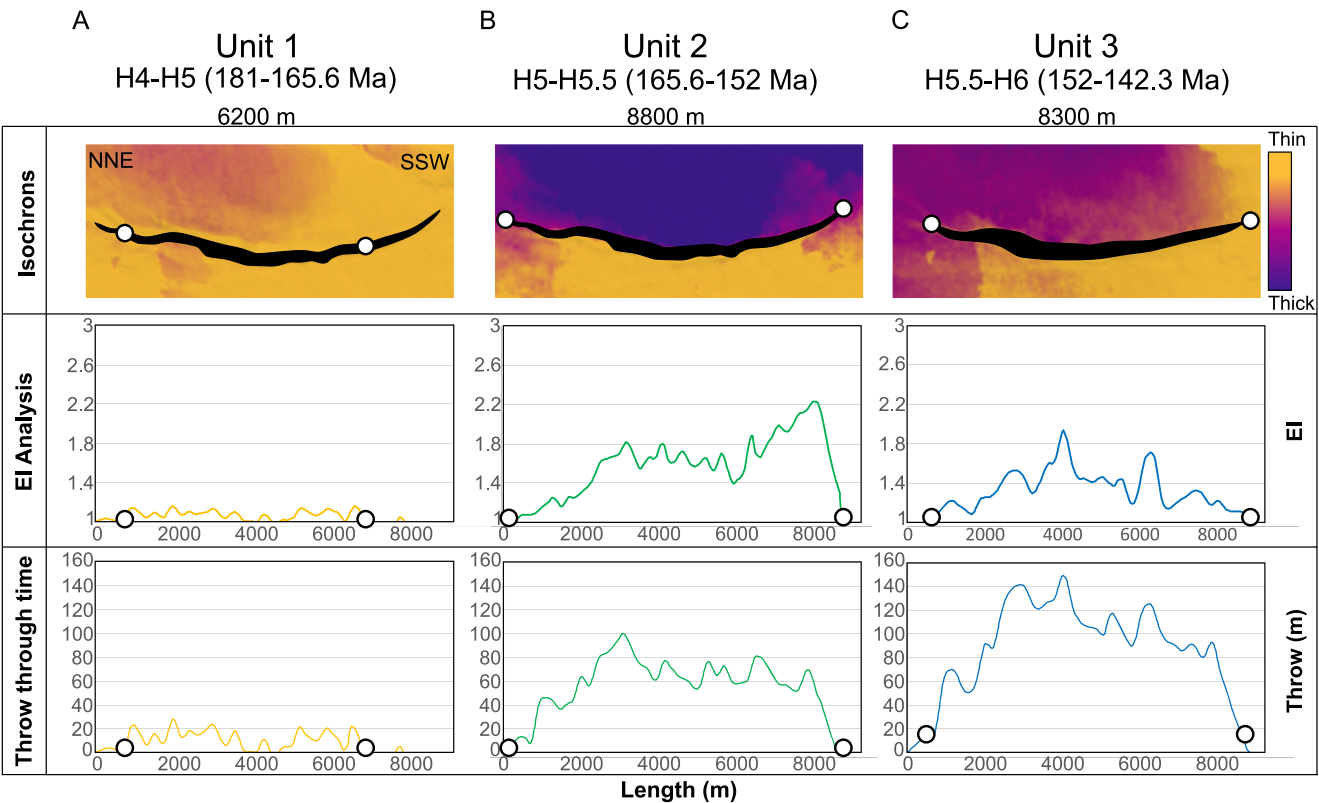


**Figure 11.** Isochrons, expansion index analysis, and throw throughout different stages of the life of F3. The throw through time values are taken from throw backstripping, which can be seen in detail in the supplementary figures. White dots indicate the length of the fault at the specified interval. (a) Isochron showing the thickness between H4 (181 Ma) and H5 (165.6 Ma), maximum throw is 28 m, and length is 6,200 m, (b) Isochron showing the thickness between H5 (165.6 Ma) and H5.5 (152 Ma), maximum throw is 100 m and length is 8,800 m, (c) Isochron showing the thickness between H5.5 (152 Ma) and H5 (142.3 Ma), maximum throw is 149 m and length is 8,300 m. All throw values could be underestimated up to 20% due to post-depositional compaction of faulted strata (Taylor et al., 2008).

There are wedge-shaped stratigraphic packages between H4 and H6 in the hanging wall, which thicken toward F3. In contrast, pre-H4 and post-H6 strata are isopachous (Figure 10a). EI values are  $\geq 1$  across a progressively longer portion of the fault from Unit 1–2 (Figures 11a and 11b), and in Unit 3, the outer tips of the fault have EI values  $< 1$  (Figure 11c).

#### 4.3.2. Interpretations

We see across-fault hanging wall thickening between H4 and H6 (Units 1–3) in cross section (Figure 10a) and in isochron thickness maps (Figures 11a–11c), suggesting F3 was active from c. 181 Ma to 142.3 Ma (Early Jurassic–Early Cretaceous). F3 likely initiated along its central segment during Unit 1 and reached its maximum length by the time of deposition of Unit 2 (Figure 11b); this is clearly evidenced by EI values  $\geq 1$  along the fault's entire trace-length. Together with the overall bell-shaped (present) distribution of throw, these EI data (Figure 11) suggest F3 grew as a single fault segment, or possibly as one large fault segment that linked with a very small segment at its northern tip. During Unit 3, EI values were  $< 1$  on the northern-most part of the fault, suggesting that the F3's northern tip became inactive (Figure 11c).

In summary, according to throw backstripping and EI analysis, F3 initiated after the deposition of H4 (c. 181 Ma), and within c. 15.7 Myr (40% of its total life) was c. 6.2 km long (70.5% of maximum length). During this first phase of activity, it accumulated only 18.9% of its total throw. Approximately 13.6 Myr later, F3 propagated to its maximum length of 8.8 km. The fault had therefore reached its maximum length and accrued 67% of its total throw by this point (i.e., 75% of its life). During the last c. 9.7 Myr of the fault's life, the remaining 33% of throw was accrued, and the length of the fault shortened by 600 m on the NNE tip of the fault.

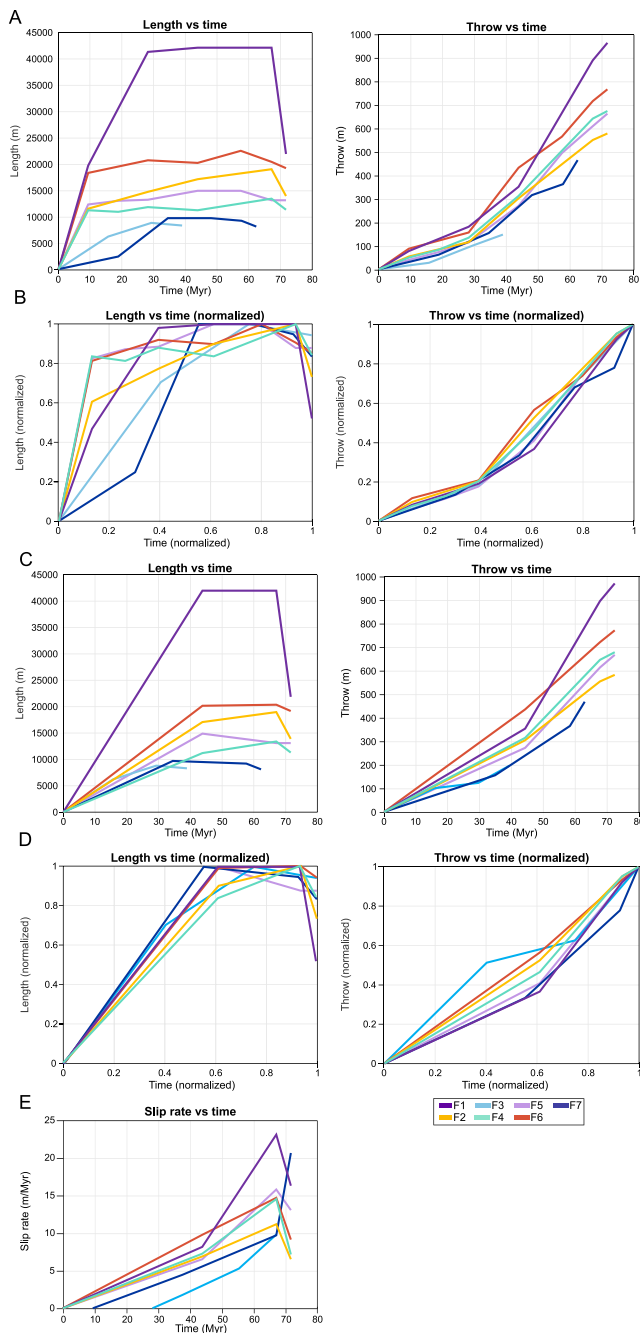


**Figure 12.** Throw and lengthening through time for F1-7 in time and normalized. The lengthening, throw/displacement, and tip retreat stages of faulting are labeled in the normalized graphs. (a–b) Throw and length through time, including all studied horizons, including H2-4 which are not age-constrained. (c–f) Throw, length, and slip rate through time, only including horizons that have been directly age-constrained. All throw values could be underestimated up to 20% due to post-depositional compaction of faulted strata (Taylor et al., 2008).

#### 4.4. Temporal Evolution of Throw and Length

All of the seven studied faults seem to have grown in three distinct stages: a lengthening stage, a throw accumulation stage, and a tip retreat stage. All of the faults had an early (i.e., first 20%–30% of their lives) relatively rapid lengthening phase, during which time they reached 60%–95% of their maximum length (see Figure 5a for isochrons across the study area, Figure 12a for values). Fault tips then grew slowly via tip propagation or segment linkage, reaching their maximum lengths after 57%–93% of their lives (Figures 5b and 5c). After they reached their maximum length, all the faults experienced a stage during which their overall at-surface trace-lengths reduced by up to 2.5 km (up to 25% of their total length) (Figures 12a and 12b). Three-stage fault growth can also be seen in additional faults in Figure 5.

Because of these shared kinematics, all of the faults studied displayed similar temporal changes in their throw-length scaling relationship (Figures 12b and 12c). The three-stage kinematics identified above also correlated with changes in throw (Figures 12b and 12d) and slip rate (Figure 12e). For example, during the lengthening stage, slip rate was relatively low ( $1.8 + 0.51$ – $9.7 + 2.0$  m/Myr). During the subsequent throw accumulation stage, there was an abrupt increase in slip rate (to  $5.3 + 1.0$ – $23 + 4.6$  m/Myr). Slip rate decreased slightly ( $6.5 + 1.2$ – $20.7 + 4.8$  m/Myr) as the faults died. It should be noted that the slip rate during the first half of the fault’s life (until deposition of H5) is likely underestimated due to the basin being somewhat sediment starved during this period. A higher slip rate would mean the time difference between the lengthening and throw accumulation stages is smaller.

### 5. Discussion

#### 5.1. Implications for Fault Growth Models

Our study identifies three key stages of fault growth on the Exmouth Plateau, offshore NW Australia. First, there was an initial lengthening stage; all of the faults reached 60%–95% of their maximum length within the first 20%–30% of their lives (Figure 13a). Maximum length was later reached via tip propagation or segment linkage. Second, there was then a throw accumulation stage that lasted from ~30%–75% of the faults’ lives; during this time, faults lengthened very little and experienced an increased slip rate (Figure 13b). Third, the tip retreat stage, which that lasted for the final 25% of the faults’ lives, and during which the faults experienced tip-line retreat and throw was partitioned toward the center of the fault (Figures 13c and 13d). Our findings are generally consistent with the model of Rotevatn et al. (2019), with two exceptions. First, the fault maximum length is not always reached during the initial lengthening stage; that is, our results demonstrate that, while the bulk of lengthening happens relatively quickly, 5%–40% can subsequently occur during lateral tip propagation and/or segment linkage. Variations in when a fault reached its maximum length was likely controlled by whether a fault links with a nearby segment or not, a process perhaps dictated by the ability of the faults to breach intervening relays. Second, there was a stage of tip retreat, a behavior characterizing the end of life of all the studied faults (Figures 13c and 13d). Further work on normal faults imaged in 3D seismic reflection data may reveal this is a more common aspect of normal fault behavior than currently thought, meaning this stage of fault growth or more precisely, death, could be included in general fault evolution models (Nicol et al., 2020).

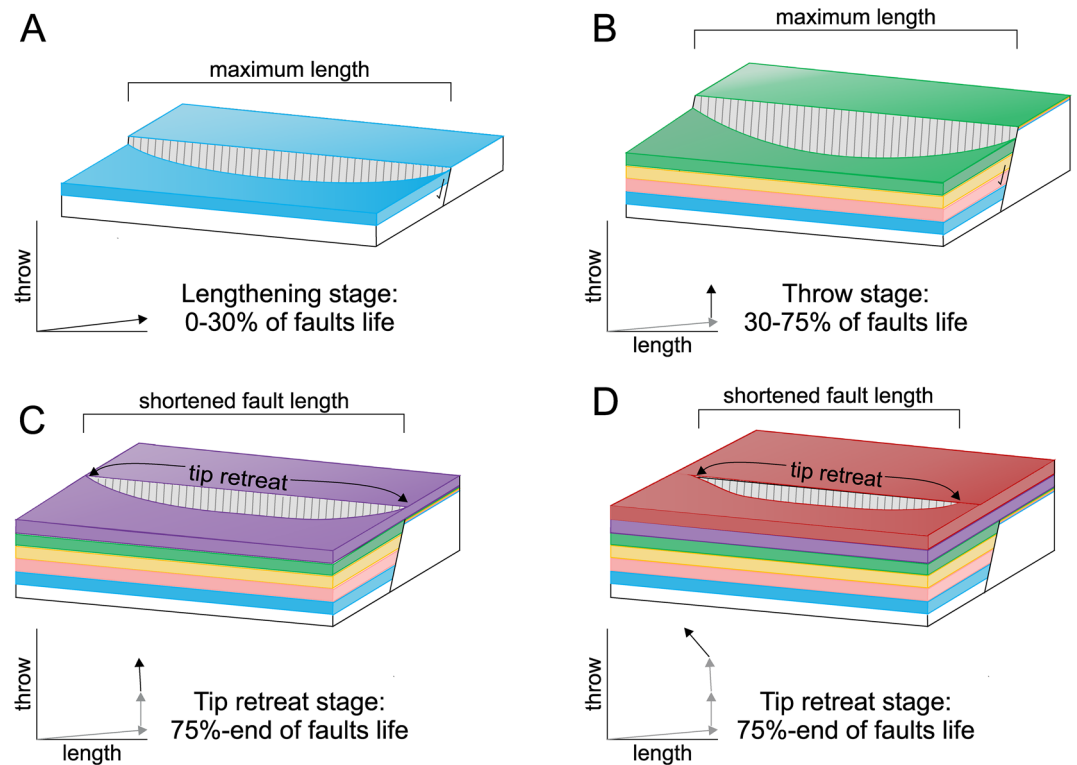


**Figure 13.** Schematic models showing the phases of fault growth. (a) Fault lengthening stage, when faults establish their near-maximum length within the first 30% of their lives (b) Fault throw accrual stage, where faults have already reached their maximum length, and throw rate increases (c) the beginning of the tip retreat stage, where the tips of the fault become inactive and (d) the continuation of the tip retreat stage, where the active fault trace line is progressively shorter.

## 5.2. The Role of Tip Retreat

Fault tip retreat was present on one or both tips of all of the faults in our study. This process has, however, only very rarely been described. Meyer et al. (2002) note a stage of tip retreat on Tertiary normal faults in the Vulcan Sub-basin, NW Shelf, Australia. The reasons why fault tips might retreat may have been overlooked because of a historical focus on how normal faults grow as opposed to how they die, and/or because high-quality, age-constrained seismic reflection data, with numerous mappable horizons within fault-related growth strata, are not available.

All of the studied faults decreased in length (by up to 2.5 km, or 25% of their trace-length) during the last 14 million years (25%) of their lives by retreat of one or both of their lateral tips. This could be explained by two hypotheses. The first hypothesis is that the faults were experiencing late-stage *true* tip retreat; that is, strain became localized near the fault center, leading to progressively shorter surface trace. We would expect that fault surface ruptures shortened as the fault gets closer to death (Figure 14a). An alternate hypothesis is that tip-line retreat was only *apparent* and was related to the faults having an elliptical geometry during the later stages of faulting, due to it having a plunging upper tip-line (i.e., during deposition of H5-7; Figure 14b). In this scenario, the fault would have intersected the free-surface along progressively shorter trace-lengths, with the fault tips being blind (Figure 13b). An increase in sediment accumulation rate relative to fault slip rate could drive this progression. The fault geometries associated with both hypotheses would look similar in seismic data (Figures 14a and 14b).

We argue that we are seeing true fault tip retreat because if retreat was only apparent and related to the faults elliptical shape, we would expect vertical throw gradients across the horizons to be similar to those encountered on blind normal faults (Childs et al., 2003; Meyer et al., 2002; Walsh & Watterson, 1988). For a blind fault, only modest strain can be accommodated by the rock volume without upward tip propagation.



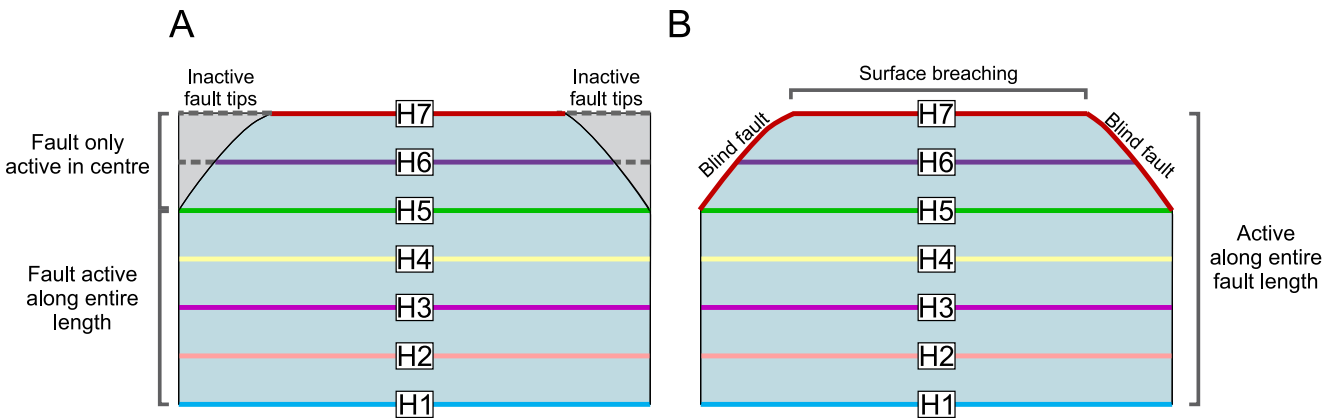


**Figure 14.** Schematics showing two possibilities for the apparent tip line retreat in this study. Fault planes along dip are shown, and colored lines indicate the active length of the fault at the time of the deposition of the associated horizons (H1-7). (a) Fault length remains constant from H1-5 and becomes active a progressively shorter distances across H6 and H7, which can be interpreted as lateral tip retreat. (b) The fault remains active across the entire length of the fault, but in the later stages of faulting (H6-7) the fault only breaches the surface in the center of the fault, and the fault tips remain active at depth, acting as blind faults.

In the case of the upper tip of a blind fault, a maximum vertical displacement gradient of  $<0.1$  is typical (Baudon & Cartwright, 2008; Childs et al., 2003; Meyer et al., 2002; Walsh & Watterson, 1988). We measured the maximum vertical displacement gradients between H6 and H7 in the center of the faults and found values between 0.08-4.5 (Figures 6, 8, and 10b), which is higher than that typically found for blind faults (Walsh & Watterson, 1988) (Figure 13). Such high vertical displacement gradients suggest that the *entire length* of the upper tip-line must have intersected the free-surface (Baudon & Cartwright, 2008; Childs et al., 2003; Meyer et al., 2002), and that a portion of the fault had become inactive during the later stages of the fault's life, before the deposition of H6 and H7.

When verifying that the tip retreat we see is real, it is important to ensure that the faults are not sediment-starved during the latter stages of their development (post-Jurassic). A reported example of possible tip retreat comes from the East African Rift (Morley, 2002); however, in this case it is possible that the faults became inactive earlier than assumed, and what appears to be tip retreat is only (passive) sediment filling of a starved basin. In our study, we argue the faults were not sediment-starved at the end of their lives (Berriasi-Hauterivian), given appreciable amounts of sediment were deposited in the footwall of the faults during deposition of H5 to H7 (Figures 6a, 7a, and 9a).

### 5.3. Slip Rates and Slip Rate Variability

We document a distinct, order-of-magnitude increase in slip rates from as little as 4 m/Myr to as much as 23 m/Myr, some 40-50 Mya after the studied faults initiated, around the time of the deposition of H5 (c. 165.6 Ma). These rates fall toward the lower end of long-term slip rates determined from the analysis of seismic reflection data imaging other natural extensional basins in a range of geodynamic setting (e.g., 4-1,000 m/Myr; Nicol et al., 1997). However, these rates are broadly consistent with rates calculated over the relatively long timescales (i.e.,  $>40$  Myr) considered here (i.e., 25 m/Myr; North Sea example in Figure 2 in Nicol et al., 1997). We note that the increase in slip rates in our NW Shelf examples temporally correspond to a time when many of the minor faults became inactive (see minor faults that tip-out below H5; Figures 4 and 5a-5c), when strain localized onto the large faults presently defining the basin structure. Similar relationships between increasing fault slip rates (or related subsidence rates) and strain localization are documented in several other natural rifts (e.g., Gawthorpe et al., 2003) and are reproduced in numerical models (e.g., Cowie & Roberts, 2001; Gupta & Scholz, 1998), with this relationship thought to reflect stress-feedback interactions during fault system growth. Long-term fluctuations in slip rate could also reflect changes in regional strain rate, related to the fundamental plate-driven processes driving deformation (Mouslopoulou et al., 2009; Nicol et al., 1997). More specifically, the marked increase in slip rates could reflect an increase in regional strain rate associated with rifting and, ultimately, continental break-up. However, we cannot

independently constrain the rate of plate boundary processes during the time interval considered here (i.e., Middle Jurassic to Early Cretaceous), principally because the time-equivalent margin facing the NW Shelf is not preserved.

## 6. Conclusions

We use 3D seismic data from offshore NW Australia to study normal fault growth through time. We show that the majority of the studied faults had three distinct stages of fault evolution. During the first stage, the “lengthening stage,” the faults accumulated at least between 60%–95% of their final length and accrued between 10%–20% of throw. This stage lasted for up to 30% of the faults’ lives. The second stage, termed the “throw stage,” fault slip rate increased, and the remainder of maximum fault length was reached. We also suggest that these faults had a third stage of fault growth, the “tip retreat stage,” where the active trace line of the fault decreases by up to 25% and throw continues to be accrued. More evidence is needed to determine how prevalent tip retreat is, but it could be an important part of late stage fault growth and possibly should be included in future fault growth models.

## Data Availability Statement

The Glencoe 3D seismic data set and associated wells can be downloaded from <https://www.ga.gov.au/nopims> by searching for the survey “Glencoe” in the data access search engine.

## Acknowledgments

The authors thank Imperial College for providing B. Lathrop with the Presidential scholarship to fund their PhD research. The authors thank Geoscience Australia for making all of the data used in this study publicly available. The authors thank Schlumberger for providing access to Petrel software. The authors also thank the Imperial College Basins Research Group (BRG) for their input and help throughout this research, and many colleagues with whom we have had beneficial conversations with at EGU and TSG conferences. The authors thank Telemaco Tesesi and two anonymous reviewers for their constructive feedback, which helped improve the final version of this paper.

## References

- Baudon, C., & Cartwright, J. A. (2008). 3D seismic characterization of an array of blind normal faults in the Levant Basin, Eastern Mediterranean. *Journal of Structural Geology*, 30(6), 746–760. <https://doi.org/10.1016/j.jsg.2007.12.008>
- Bilal, A., Mcclay, K. E. N., & Scarselli, N. (2018). Fault-scarp degradation in the central Exmouth Plateau, North West Shelf, Australia. *Geological Society, London, Special Publications*, 476(1), 231–257.
- Bouroulllec, R., Cartwright, J. A., Johnson, H. D., Lansigu, C., Quémener, J.-M., & Savanier, D. (2004). Syndepositional faulting in the Grès d'Annot Formation, SE France: High-resolution kinematic analysis and stratigraphic response to growth faulting. *Geological Society, London, Special Publications*, 221, 241–265. <https://doi.org/10.1144/gsl.sp.2004.221.01.13>
- Brown, A. R. (2011). *Interpretation of three-dimensional seismic data*. Tulsa, OK: AAPG Memoir 42. SEG Investigation in Geophysics, 9(42).
- Cartwright, J., Bouroulllec, R., James, D., & Johnson, H. (1998). Polycyclic motion history of some Gulf Coast growth faults from high-resolution displacement analysis. *Geology*, 26(9), 819–822. [https://doi.org/10.1130/0091-7613\(1998\)026<0819:PMHOSG>2.3.CO;2](https://doi.org/10.1130/0091-7613(1998)026<0819:PMHOSG>2.3.CO;2)
- Cartwright, J. A., Trudgill, B. D., & Mansfield, C. S. (1995). Fault growth by segment linkage: An explanation for scatter in maximum displacement and trace length data from the Canyonlands Grabens of SE Utah. *Journal of Structural Geology*, 17(9), 1319–1326. [https://doi.org/10.1016/0191-8141\(95\)00033-A](https://doi.org/10.1016/0191-8141(95)00033-A)
- Chapman, T. J., & Menelly, A. W. (1991). The displacement patterns associated with a reverse-reactivated, normal growth fault. *Geological Society, London, Special Publications*, 56, 183–191. <https://doi.org/10.1144/gsl.sp.1991.056.01.12>
- Childs, C., Holdsworth, R. E., Jackson, C. A.-L., Manzocchi, T., Walsh, J. J., & Yielding, G. (2017). *Introduction to the geometry and growth of normal faults*. London: Geological Society Special Publications. SP439.23. <https://doi.org/10.1144/SP439.24>
- Childs, C., Nicol, A., Walsh, J. J., & Watterson, J. (2003). The growth and propagation of synsedimentary faults. *Journal of Structural Geology*, 25(4), 633–648. [https://doi.org/10.1016/S0191-8141\(02\)00054-8](https://doi.org/10.1016/S0191-8141(02)00054-8)
- Cowie, P. A., & Roberts, G. P. (2001). Constraining slip rates and spacings for active normal faults. *Journal of Structural Geology*, 23(12), 1901–1915. [https://doi.org/10.1016/S0191-8141\(01\)00036-0](https://doi.org/10.1016/S0191-8141(01)00036-0)
- Cowie, P. A., & Shipton, Z. K. (1998). Fault tip displacement gradients and process zone dimensions. *Journal of Structural Geology*, 20(8), 983–997. [https://doi.org/10.1016/S0191-8141\(98\)00029-7](https://doi.org/10.1016/S0191-8141(98)00029-7)
- Dawers, N. H., Anders, M. H., & Scholz, C. H. (1993). Growth of normal faults: Displacement-length scaling. *Geology*, 21(12), 1107–1110. [https://doi.org/10.1130/00917613\(1993\)021<1107:GONFDL>2.3.CO;2](https://doi.org/10.1130/00917613(1993)021<1107:GONFDL>2.3.CO;2)
- Fossen, H., & Rotevatn, A. (2016). Fault linkage and relay structures in extensional settings—A review. *Earth-Science Reviews*, 154, 14–28. <https://doi.org/10.1016/j.earscirev.2015.11.014>
- Freitag, U. A., Sanderson, D. J., Lonergan, L., & Bevan, T. G. (2017). Comparison of upwards playing and upwards merging segmented normal faults. *Journal of Structural Geology*, 100, 1–11. <https://doi.org/10.1016/j.jsg.2017.05.005>
- Gawthorpe, R. L., Jackson, C. A.-L., Young, M. J., Sharp, I. R., Moustafa, A. R., & Leppard, C. W. (2003). Normal fault growth, displacement localisation and the evolution of normal fault populations: The Hammam Faraun fault block, Suez rift, Egypt. *Journal of Structural Geology*, 25, 883–895. [https://doi.org/10.1016/S0191-8141\(02\)00088-3](https://doi.org/10.1016/S0191-8141(02)00088-3)
- Gibbons, A. D., Barkhausen, U., Bogaard, P. Van Den, Hoernle, K., Werner, R., Whittaker, J. M., & Müller, R. D. (2012). Tectonic evolution of the West Australian margin. *Geochemistry, Geophysics, Geosystems*, 13, 1–25. <https://doi.org/10.1029/2011GC003919>
- Gupta, A., & Scholz, C. H. (1998). Utility of elastic models in predicting fault displacement fields. *Journal of Geophysical Research*, 103, 823–834. <https://doi.org/10.1029/97jb03009>
- Hemelsdaël, R., & Ford, M. (2016). Relay zone evolution: A history of repeated fault propagation and linkage, central Corinth rift, Greece. *Basin Research*, 28, 34–56. <https://doi.org/10.1111/bre.12101>
- Henstra, G. A., Rotevatn, A., Gawthorpe, R. L., & Ravnås, R. (2015). Evolution of a major segmented normal fault during multiphase rift-ing: The origin of plan-view zigzag geometry. *Journal of Structural Geology*, 74, 45–63. <https://doi.org/10.1016/j.jsg.2015.02.005>

- Jackson, C. A.-L., Bell, R. E., Rotevatn, A., & Tvedt, A. B. M. (2017). *Techniques to determine the kinematics of synsedimentary normal faults and implications for fault growth models*. London: Geological Society Special Publications. SP439.22. <https://doi.org/10.1144/SP439.22>
- Jackson, C. A.-L., & Rotevatn, A. (2013). 3D seismic analysis of the structure and evolution of a salt-influenced normal fault zone: A test of competing fault growth models. *Journal of Structural Geology*, 54, 215–234. <https://doi.org/10.1016/j.jsg.2013.06.012>
- Longley, I. M., Buessenschuett, C., Clydsdale, L., Cubitt, C. J., Davis, C. J., Johnson, R. C., et al. (2002). The north west shelf of Australia – A woodside perspective. *Proceedings of the petroleum exploration society of Australia symposium*, 27–88.
- Marshall, N. G., & Lang, S. C. (2013). A New Sequence Stratigraphic Framework for the North West Shelf, Australia. *The sedimentary basins of Western Australia 4: Proceedings PESA symposium*, 1–32.
- Meyer, V., Nicol, A., Childs, C., Walsh, J. J., & Watterson, J. (2002). Progressive localisation of strain during the evolution of a normal fault population. *Journal of Structural Geology*, 24(8), 1215–1231. [https://doi.org/10.1016/S0191-8141\(01\)00104-3](https://doi.org/10.1016/S0191-8141(01)00104-3)
- Morley, C. K. (2002). Evolution of large normal faults: Evidence from seismic reflection data. *AAPG Bulletin*, 86(6), 961–978. <https://doi.org/10.1306/61EEDBFC-173E-11D7-8645000102C1865D>
- Morley, C. K., Nelson, R. A., Patton, T. L., & Munn, S. G. (1990). Transfer zones in the East African rift system and their relevance to hydrocarbon exploration in rifts. *AAPG Bulletin*, 74(8), 1234–1253. <https://doi.org/10.1306/0C9B2475-1710-11D7-8645000102C1865D>
- Mouslopoulou, V., Walsh, J. J., & Nicol, A. (2009). Fault displacement rates on a range of timescales. *Earth and Planetary Science Letters*, 278(3–4), 186–197. <https://doi.org/10.1016/j.epsl.2008.11.031>
- Nicol, A., Childs, C., Walsh, J. J., Manzocchi, T., & Schöpfer, M. P. J. (2016). Interactions and growth of faults in an outcrop-scale system. *Geological Society, London, Special Publications*, 439, 23–39. <https://doi.org/10.1144/SP439.9>
- Nicol, A., Walsh, J., Berryman, K., & Nodder, S. (2005). Growth of a normal fault by the accumulation of slip over millions of years. *Journal of Structural Geology*, 27(2), 327–342. <https://doi.org/10.1016/j.jsg.2004.09.002>
- Nicol, A., Walsh, J., Childs, C., & Manzocchi, T. (2020). *The growth of faults. Understanding Faults*. Elsevier Inc. <https://doi.org/10.1016/B978-0-12-815985-9.00006-0>
- Nicol, A., Walsh, J. J., Watterson, J., & Underhill, J. R. (1997). Displacement rates of normal faults. *Nature*, 390, 157–159. <https://doi.org/10.1038/36548>
- Nugraha, H. D., Hodgson, D. M., Reeve, M. T., Jackson, C. A. L., & Johnson, H. D. (2019). Tectonic and oceanographic process interactions archived in Late Cretaceous to Present deep-marine stratigraphy on the Exmouth Plateau, offshore NW Australia. *Basin Research*, 31(2018), 405–430. <https://doi.org/10.1111/bre.12328>
- Pan, S., Bell, R., Jackson, C. A. L., & Naliboff, J. (2020). *Evolution of normal fault displacement and length as the continental lithosphere stretches*. <https://doi.org/10.31223/osf.io/h7cjd>
- Peacock, D. C. P., & Sanderson, D. J. (1994). Geometry and development of relay ramps in normal fault systems. *American Association of Petroleum Geologists*, 78(2), 147–165. <https://doi.org/10.1306/BDF9046-1718-11D7-8645000102C1865D>
- Peterson, K., Clausen, O. R., & Korstgard, J. A. (1992). Evolution of a salt-related listric growth fault near the D-1 well, block 5605, Danish North Sea: Displacement history and salt kinematics. *Journal of Structural Geology*, 14(5), 565–577. [https://doi.org/10.1016/0191-8141\(92\)90157-R](https://doi.org/10.1016/0191-8141(92)90157-R)
- Pickering, G., Peacock, D. C. P., Sanderson, D. J., & Bull, J. M. (1996). Modeling tip zones to predict the throw and length characteristics of faults. *AAPG Bulletin*, 81(1), 82–99. <https://doi.org/10.1306/522B4299-1727-11D7-8645000102C1865D>
- Rotevatn, A., Jackson, C. A. L., Tvedt, A. B. M., Bell, R. E., & Blækkann, I. (2019). How do normal faults grow? *Journal of Structural Geology*, 125, 173–184. <https://doi.org/10.1016/j.jsg.2018.08.005>
- Stagg, H. M. J., & Colwell, J. B. (1994). The Structural Foundations of the Northern Carnarvon Basin. In *The sedimentary basins of Western Australia: Proceedings of petroleum exploration society of Australia symposium, Perth* (pp. 349–372).
- Stagg, H. M. J., Colwell, J. B., Direen, N. G., O'Brien, P. E., Bernardel, G., Borissova, I., et al. (2004). Geology of the continental margin of Enderby and Mac. Robertson Lands, East Antarctica: Insights from a regional data set. *Marine Geophysical Researches*, 25, 183–219. <https://doi.org/10.1007/s11001-005-1316-1>
- Taylor, S. K., Nicol, A., & Walsh, J. J. (2008). Displacement loss on growth faults due to sediment compaction. *Journal of Structural Geology*, 30(3), 394–405. <https://doi.org/10.1016/j.jsg.2007.11.006>
- Thorsen, C. E. (1963). Age of growth faulting in Southeast Louisiana. *Gulf Coast Association of Geological Societies Transactions*, 3, 103–110.
- Tindale, K., Newell, N., Keall, J., & Smith, N. (1998). Structural Evolution and Charge History of the Exmouth Sub-basin, Northern Carnarvon Basin, Western Australia. *The sedimentary basins of Western Australia 2: Proceedings of petroleum exploration society of Australia symposium*.
- Tvedt, A. B. M., Rotevatn, A., & Jackson, C. A.-L. (2016). Supra-salt normal fault growth during the rise and fall of a diapir: Perspectives from 3D seismic reflection data, Norwegian North Sea. *Journal of Structural Geology*, 91, 1–26. <https://doi.org/10.1016/j.jsg.2016.08.001>
- Velayatham, T., Holford, S. P., Bunch, M., King, R. C., & Magee, C. (2019). 3D seismic analysis of ancient subsurface fluid flow in the exmouth plateau, offshore western Australia. *The sedimentary basins of Western Australia V: Proceedings of the petroleum exploration society of Australia symposium*.
- Walsh, J. J., Bailey, W. R., Childs, C., Nicol, A., & Bonson, C. G. (2003). Formation of segmented normal faults: A 3-D perspective. *Journal of Structural Geology*, 25(8), 1251–1262. [https://doi.org/10.1016/S0191-8141\(02\)00161-X](https://doi.org/10.1016/S0191-8141(02)00161-X)
- Walsh, J. J., Nicol, A., & Childs, C. (2002). An alternative model for the growth of faults. *Journal of Structural Geology*, 24(11), 1669–1675. [https://doi.org/10.1016/S0191-8141\(01\)00165-1](https://doi.org/10.1016/S0191-8141(01)00165-1)
- Walsh, J. J., & Watterson, J. (1988). Analysis of the relationship between displacements and dimensions of faults. *Journal of Structural Geology*, 10(3), 239–247. [https://doi.org/10.1016/0191-8141\(88\)90057-0](https://doi.org/10.1016/0191-8141(88)90057-0)
- Walsh, J. J., Watterson, J., Bailey, W. R., & Childs, C. (1999). Fault relays, bends and branch-lines. *Journal of Structural Geology*, 21(8–9), 1019–1026. [https://doi.org/10.1016/S0191-8141\(99\)00026-7](https://doi.org/10.1016/S0191-8141(99)00026-7)
- Wilkinson, M., Roberts, G. P., McCaffrey, K., Cowie, P. A., Faure Walker, J. P., Papanikolaou, I., et al. (2015). Slip distributions on active normal faults measured from LiDAR and field mapping of geomorphic offsets: An example from L'Aquila, Italy, and implications for modeling seismic moment release. *Geomorphology*, 237, 130–141. <https://doi.org/10.1016/j.geomorph.2014.04.026>
- Wilson, P., Elliott, G. M., Gawthorpe, R. L., Jackson, C. A.-L., Michelsen, L., & Sharp, I. R. (2013). Geometry and segmentation of an evaporite-detached normal fault array: 3D seismic analysis of the southern Bremstein Fault Complex, offshore mid-Norway. *Journal of Structural Geology*, 51, 74–91. <https://doi.org/10.1016/j.jsg.2013.03.005>